A New Approach to Determine Material Characteristics Using Spherical Indentation and Neural Networks

A.H. Mahmoudi[a1] , S.H. Nourbakhsh[a] and R. Amali[b]
[a] Department of Mechanical Engineering, Faculty of Engineering, University of Bu-Ali Sina, Hamedan, Iran.
[b] Department of Engineering Design and Mathematics, University of West of England, Bristol, BS16 1QY, UK.

Abstract:

Material characteristics such as Young modulus, yield and ultimate stresses are often considered as fundamental material parameters. Determination of material characteristics using the instrumented indentation test has been gained interests among many researchers. The output of a spherical indentation test is usually the load-penetration (P-h) curve which is used to determine the Hollomon's equation coefficients. Ideally, the elastic deformation of the sphere is to be excluded from the total displacement. However, the available techniques to omit the elastic deformation of the sphere are difficult-to-use and time consuming.

In the present work, a noticeably simplified method is proposed preserving the required accuracy. The coefficients of Hollomon's equation were determined using the spherical indentation. The proposed method has also the ability to specify the unloading curve at each point of interest, even if the experimental data of the unloading procedure at that point is not available. Finally, by training a Neural Network and extracting the weights of its layers, an equation governing the network is presented explicitly. This expression made the neural network easy to use. Furthermore, the proposed method was verified using the experimental results and very good agreements were observed.

Keywords: *Material characteristics, Yield stress, Spherical Indentation, Hardness test, Neural Networks.*

[1] Corresponding author: Email: a.h.mahmoudi@gmail.com, Tel: +98 811 8257410, FAX: +98 811 8257400.

Nomenclature

P	Force (N)
h	Displacement (mm)
σ	Stress (MPa)
E	Young Modulus (MPa)
ε	Strain
a	Contact radius
ν_i	Poisson ratio of indenter
ν_s	Poisson ratio of sample
E^*	Reduced Young Modulus
E_i	Young Modulus of indenter
E_s	Young Modulus of sample
S	Slope
h_{p_i}	Real amount of penetration
h_{p_0}	Superficial amount of penetration
R	Radius of indenter
$\delta = h_{p_0} - h_{p_1}$	Difference between real and superficial amount of penetration
W_t	Plastic energy
α_i	Output for the i^{th} cell
X_j	Input For The i^{th} cell
W_{ij}	Weight
t_j	Target output
O_j	Corresponding output
IW	Weight in the first layer
LW	Weight in the second layer
b	Biases

1 Introduction:

Tensile tests are usually carried out to characterize the material parameters. Preparing the standard coupons for the tests is destructive, expensive and difficult. A cheap and simple non-destructive method to determine the material characteristics, which has been widely developed in the literature, is the instrumented indentation test also known as hardness test [1, 2 and 3]. The instrumented

indentation test provides an accurate load (P) versus penetration depth (h) curve. The P–h curve is sensitive to variety of different test details. However, it is mainly influence by the uniaxial stress–strain curve of the material. It may also be used in order to determine some parameters of the work-hardening behavior of the material. Hollomon isotropic work-hardening law is the most commonly used stress-strain curve and is defined as:

$$\sigma = \sigma_y^{1-n} E^n \varepsilon^n \tag{1}$$

where E, σ_y , n and ε, are the Young modulus, the yield stress, the work-hardening exponent and the strain respectively. Researchers have used the slope of the P–h curve during loading process to estimate plastic flow properties and deduced the Young Modulus from the unloading slope [4, 5]. Pharr and Oliver [5] obtained E^* from an indentation test using Equation (2):

$$S = \frac{dP}{dh} = 2E^* a \tag{2}$$

where a is the contact radius, E^* is the reduced Young modulus and defined as:

$$E^* = \left[\frac{1-\nu_i^2}{E_i} + \frac{1-\nu_s^2}{E_s} \right]^{-1} \tag{3}$$

where ν is the Poisson ratio, E_s and E_i are the Young modulus of the sample and the indenter respectively. They performed a comparison between the numerical and experimental results and showed that equation (2) did not lead to a very accurate estimation of the contact radius. However, it predicted the trend of the contact radius alterations. This can be a result of using the simplified material properties in the numerical simulations that did not correspond to the real material behavior. Furthermore, equation (2) did not take into account the radial displacements of material under the indenter [6]. Hay and Wolff [7] then introduced a factor of γ and the contact stiffness equation became:

$$S = \frac{dP}{dh} = \frac{2\gamma E_s a}{1-\nu_s^2} \qquad (۴)$$

For an elastic spherical indenter, the factor of γ was defined by the following equation:

$$\gamma = 1 + \frac{2a}{3\pi R}\left[\frac{N(1-2\nu_s)(1+\nu_s)}{N(1-\nu_s^2)+(1-\nu_i^2)}\right]$$
$$N = \frac{E_i}{E_s} \qquad (۵)$$

Knowing the fact that the sphere was deformed during the penetration, the real amount of penetration (h_{pi}) was different with the superficial one (h_{p0}) as shown in Figure (1). Therefore, it was essential to substrate the deformation of the sphere from the total deformation to calculate the real amount of penetration.

Location of Figure1

Collin and his co-workers [6] proposed an empirical procedure to deduce both the indenter deformation and the contact radius using the indenter and sample elastic properties and several loading-unloading and reloading cycles. They introduced an equation [8] that omitted the deformation of sphere and resulted in the real amount of penetration. Their equation was defined as Equation (6):

$$\delta = h_{p_\circ} - h_{p_1}$$

$$\delta = R\left(A + B\frac{P}{\pi R^2}\frac{1-\nu_i^2}{E_i} + C\frac{P}{\pi a^2}\frac{1-\nu_i^2}{E_i} + D\left(\frac{P}{\pi R^2}\frac{1-\nu_i^2}{E_i}\right)^2 + E\left(\frac{P}{\pi a^2}\frac{1-\nu_i^2}{E_i}\right)^2 + F\frac{P}{\pi R^2}\left(\frac{1-\nu_i^2}{E_i}\right)^2\frac{P}{\pi a^2}\right) \qquad (6)$$

where the constant coefficients *A* to *F* were found by means of the numerical study and introduced as: *A*=-1.6517e-5, *B*=3.6242, *C*=0.2003, *D*=-7784.7622, *E*=-15.3689 and *F*=649.4548. *P*, υ, *R*, E_i and *a* are the force, Poisson ratio, the radius of the sphere, Young modulus of the sphere and the contact radius, respectively. h_{p0} and h_{p1} were illustrated earlier in Figure 1.

Two approaches may be used to extract mechanical properties from the indentation test. The first is based on the inversion of models established from a numerical study and is called a "reverse" analysis. The second is based on an "inverse" analysis. In the reverse analysis, a set of data is achieved from numerical simulations. A reverse relation is then obtained by correlating the data acquired from the p-h diagram and the stress-strain curve of the sample. Different information is extracted from the p-h diagram depending on how the loading trend appeared. For instance in cyclic loading, information such as changes in elastic and plastic energy and force changes versus changes in the amount of penetration could be extracted. Collin et al. [9] presented a reverse method to determine the stress-strain curve of the sample by finding the relationship between the data from the P-h diagram of cyclic loading and the stress-strain curve. They cyclically loaded the sample up to 200N and determined the changes of plastic energy versus *h*. Finally, coefficients A and B were specified by fitting the equation (7) to the data.

$$\frac{W_t}{E^* R^3} = \left(\frac{h}{R}\right)^A \exp(-B) \tag{7}$$

Having coefficients A and B calculated, the work-hardening exponent and the yield stress of the material in the Hollomon's equation is determined by fitting equation (8) to the numerical data.

$$A = \frac{a + bx + cx^2 + dx^3 + ey + fy^2}{1 + gx + hx^2 + ix^3 + jy} \qquad B = \frac{a + cx + ey + gx^2 + iy^2 + kxy}{1 + bx + dy + fx^2 + hy^2 + jxy} \tag{8}$$

$$x = \frac{\sigma_y}{E^*} \qquad y = n$$

	a	b	c	d	e	F	g	h	i	j	k
For A	1.9315	526.624	−45734.4050	1096080	5.1262	0.7832	212.8758	−19375.6920	468759.1	2.1066	-
For B	5.7879	405.2397	392.1503	−0.6645	−11.3579	−4573.9157	−14009.3360	−1.8652	2.2474	−215.9234	**−192.3363**

Table 1: Coefficients A and B in equation (8).

Tyulyukovskiy and Hobber [10] employed finite element analysis of the spherical indentation and neural networks to determine the plastic and visco-plastic properties of the sample. They also

corrected the P-h diagram obtained from the experiments using neural networks [11]. However, their technique only provided appropriate results for bulk materials and thin films.

In the present work, a new technique that considerably simplified the current methods to eliminate the elastic deformation of the sphere is proposed. Material properties were then determined from the p-h diagram using neural networks. Finally, for explicit use of the results, a relation based on the neural networks weights is introduced. The neural networks theory is detailed next as it was employed to determine the parameters in this research.

2 Artificial Neural Networks

The neural networks are essentially connectionist systems in which neurons are connected to each other. A neuron can provide an output signal if it receives one or more input signals. The number of signals would depend on processing function involved. Based on weights specified between network layers, the output is transferred to other neurons with different intensities. The outputs of neurons of a layer are inputs to the neurons of the next layer. The first layer, namely input layer, receives the data from the user and the last layer, which is called output layer, prepare the output data for the user. The middle layers are called hidden layers. The presence of hidden layers provides complexity for the network architecture and this complexity is employed for modeling nonlinear relationships.

Depending on the presence or lack of feedback in the architecture of a neural network, there are two separate types of networks, namely with feedback or feed forward architectures. In a feed forward architecture, there is no returning connection from output neurons to the input neurons [12]. A network with feed forward architecture was employed in the present study.

In general, there are two different methods for training the network. There are supervised and unsupervised learning techniques. In supervised learning, an input data is related to a specified output i.e. the learning process is performed with the pairs of data. Unsupervised learning method is

used where the output or target values are unspecified [13]. Selection of the best and fastest learning algorithm for solving a problem, is very important and difficult. One of common algorithms for adjusting the weights is back-propagation algorithm. This algorithm, which is a sort of supervised learning techniques, is employed in the current work.

A network starts working with a set of initial weights and then, gradually modifies the weights in a training cycle until the desired weights are achieved. The desired weights perform the input-output mapping with the least error. The trained network is then examined with a set of data. If the testing error is greater than the training error, it can be claimed that the network possesses excessive over-fitting on the data. For a network with good over-fitting, the testing and training errors are reasonably close to each other. Now the trained neural network can be employed for estimating the outputs using a new set of data. Figure 2 shows the data processing carried out by a typical neuron of a neural network. Based on the output for the i^{th} cell, Equation (9) is defined as:

$$\alpha_i = f(\sum_{j=1}^{n} X_j W_{ij}) \tag{9}$$

The activation functions generally involve linear or nonlinear relationships. The most important step in using a neural network is the training stage.

Location of Figure2

Some statistical methods such as root mean square (RMS) error or mean square error (MSE) are employed for validation of the results. During the training stage, the error is specified by root mean square error or mean square error. In the latter case MSE is calculated by the following equation:

$$MSE = \frac{1}{n}\sum_{j=1}^{n}(t_j - O_j)^2 \tag{10}$$

In which t_j is the target value for the *j'th* output data, O_j is the corresponding output value and *n* is the number of data. A two layer neural network is presented schematically in Figure 3. In order to train the neural network a set of numerical analyses were carried out. Details of the simulations are available next.

Location of Figure 3

3 Numerical Analyses

The finite element simulation of the sphere indentation was carried out using ABAQUS finite element code [14]. An axisymmtric model of the sphere and the block of material was made. The finite element mesh was formed of 14380 CAX4R 4-noded bilinear axisymmetric elements. The finite element model and the mesh are shown in Figure 4. The material properties of two aluminum, Al7075 and Al6060, were used for this simulation with a Young's modulus of 72 GPa and a yield stress of 534 MPa for Al7075 and Young's modulus of 74 GPa and a yield stress of 302 MPa for Al6065. The Poisson ratio for both cases was considered equal to 0.3 [15]. The stress-strain curves of two aluminums are shown in Figure 5(a) [15]. Elastic-plastic properties were assumed with isotropic linear hardening. Hollomon's equation was employed to characterize the two materials behavior in the plastic region (see equation 1). The coefficient *n* in equation (1) was considered equal to 0.061, 0.071 for Al 6065 and Al 7075 respectively. All nodes on the lower boundary of the mesh were constrained so that they were free in the radial direction and fixed in the axial direction. Uniform axial loading was applied to the top surface of the sphere.

The sphere was simulated using 9620 CAX4R 4-noded bilinear axisymmetric elements with 600 GPa Young modulus and 0.3 Poisson ration (corresponding to Tungsten material properties). The sphere radius was 1 mm and the block of material had 60mm radius and 40mm height as illustrated in Figure 4.

Location of Figure 4

The outcomes of finite element simulations were compared with the experimental data from [15] in the form of load-penetration curves as indicated in Figure 5(b). It can be seen that the comparison showed a very good correlation between the experimental data and those predicted for both alloys.

Location of Figure 5

Gaining confidence on the finite element results, a series of simulations were carried out to cover a wide range of different materials. The simulations were repeated using material properties with yield stresses of 150, 450, 720, 1000, 1400, 2200 and 3000 MPa. Furthermore, a wide range of coefficient n in the Hollomon's equation was employed equal to 0.02, 0.08, 0.15, 0.22, 0.28, 0.34 and 0.4. In total 49 analyses were performed. These simulations were utilized to train the neural network and will be discussed later. Available methods in the literature to separate the elastic deformation of the sphere from the P-h curve are discussed in more details next.

4 Determination of $P-h_{p_1}$ curve from $P-h_{p_0}$ curve

4.1 Available procedure in the literature

As mentioned earlier, the elastic deformation of the sphere that causes the true penetration is different from the measured one which corresponds to the displacement of the sphere centre. Therefore, it is essential to work out the sphere elastic deformation in both loading and unloading. This deformation is then subtracted from the displacement of the sphere centre to achieve the true penetration. Collin and his co-workers [6 and 8] introduced a procedure in which the corrected sphere displacement was achieved using cyclic loading and unloading. They then subtracted the sphere elastic deformation from the raw data. The sequence of their method is as follow; first they estimated an arbitrary *a-h* diagram (contact area versus penetration curve). Second, the equivalent

radius, $R_{eq}(a)$, was determined using *a-h* diagram as the indenter never had the exact spherical shape. Next, $P(h_{p_0})$, R_{eq} and *a-h* curves and the amount of penetration, *δ-a*, was found as a curve using equation (6). The $P(h_{p_1})$ curve was then calculated using *δ-a* data and the equation of $P(h_{p_1}) = P(h_{p_0}) - \delta(a)$. Using the slope of $P(h_{p_1})$ curve and equation (4) the value of E_s was calculated. Knowing the true E_s value of the sample, true *δ-a* curve is determined by reducing the difference between the true E_s and the one found from equation (4). Having the true *δ-a* curve resulted in finding the $P(h_{p_1})$ curve. Using the above procedure the maximum points at the beginning of each unloading phase was corrected. By use of equation (11) the $P(h_{p_1})$ data in each loading process was calculated.

$$k = \frac{(h_{p_1 \max} - h_{p_0 \max})}{P_{\max}} \qquad h_{P_1} = h_{P_0} + kP \tag{11}$$

In the determination of *k*, *P* and *h* were the load and the penetration at the start point of unloading at each cycle respectively. It is fair to say that above procedure can be very long and time consuming. Furthermore, it required many loading and unloading cycles to achieve the final curve. In the present work, a new procedure was developed that minimized the efforts to obtain the load-penetration curve. The new procedure is detailed next.

4.2 The proposed procedure

In the proposed method, there was no requirement of cyclic loading. The indentation test was simply performed to a certain load level followed by unloading. The sequence of the proposed method is as follow:

1- $P(h_{P0})$ is determined up to a certain load that was obtained from the experiment and followed by unloading.

2- Using Equation (12), the slope of the unloading curve was found at the maximum point .

$$S = \frac{P_{\max} - P}{h_{P_1 \max} - h_{P_1}} = \frac{P_{\max} - P}{(h_{p_0 \max} - \delta(a)) - (h_{p_0} - \frac{\delta(a)}{P_{\max}} P)} \qquad ((۱۲)$$

where $(P_{\max}, h_{\max})$ was the start point of unloading, (P, h) was the next point on the unloading curve unloading part and $\delta(a) = h_{p_{0\max}} - h_{p_{1\max}}$.

3- Combining equations, (12), (6) and (4), a general expression for *a(h)* was found. Solving this expression led to find the contact radius where unloading began.

4- Using Equation (13), the $P(h_{p_1})$ curve was achieved from the maximum load up to 80% of the maximum load with an acceptable accuracy. The numerical analyses showed that for loads lower than 80% of the maximum load the accuracy of the equation was compromised.

$$h_{P_{1-n}} = h_{P_{0-n}} - \frac{h_{P_{0(n-1)}} - h_{P_{1(n-1)}}}{P_{(n-1)}} P_n \qquad (۱۳)$$

where *n* is the track number of the data point from which the sphere elastic deformation must be eliminated.

5- Then a curve was fitted to the data obtained from step 4 to achieve $P(h_{P1})$.

$$\frac{P}{E^* R^2} = \left(\frac{h}{R}\right)^A \exp(-B) \qquad (۱۴)$$

Knowing the fact that the slope of unloading curve was the same for each unloading cycle, the procedure below was followed.

1- The load at which the unloading cycle was required was chosen and the corresponding penetration value was found.

2- The amount of penetration on the $P(h_{p_1})$ curve was established corresponding to the load at which the unloading was occurred.

3- Two above values were subtracted.

4- To find the unloading curve from the load in step 1, the value of step 3 was subtracted from all the data points of the unloading curve that was available from unloading of the maximum load.

Location of Figure 6

The proposed technique was simple and quick. Two models were simulated using finite element method to validate both above procedures. The results are shown in Figure 6 (a) and (b). The first simulation was performed using yield stress of 450 MPa and n was equal to 0.02. In the second simulation the yield stress was kept the same and n was changed to 0.4. In both cases the maximum load was 200N. It can be seen in the figures that the proposed procedure was not sensitive to strain hardening coefficient and acceptable results were obtained for loading and unloading in each phase. As the final step of the material characterization, a neural network was employed to determine the stress-strain curve of the sample material.

5 Application of Neural Networks to Determine Stress-Strain Curve

A two-layer neural network was employed in order to find the stress-strain curve of the testing material. The first layer consisted of 7 neurons with tansig activating function. The second layer had two neurons `with purline function`. The neural network was then trained using the finite element simulations detailed in section 3 (49 simulations). Input data to the neural network were parameters A and B from equation (14) and output values were the yield stress and strain hardening coefficient in Hollomon's equation. Following training of the network for different cases, it was concluded that the best way to introduce the data to the network is to divide the yield stress by 1000 and feed it to the network along with other data.

To validate the outcomes of the neural network, the results were tested for two sets of experimental data available in [15]. Figure 7 indicates the stress-strain and load-penetration curves of two materials, AISI316L and C40 steels. Coefficients A and B for both materials were determined by fitting equation (14) to their load-penetration curve shown in the figure. Next, these coefficients were fed to the trained neural network and the coefficients of Hollomon's equation were calculated. The results are shown in Table 2. It can be seen that a good agreement was achieved between the experimental results and the neural network output.

AISI 316L				C40			
A=1.1873 B=2.456				A=1.2007 B=1.9449			
EXP.		Neural network		EXP.		Neural network	
n	σ_y	n	σ_y	n	σ_y	n	σ_y
0.278	148	0.2581	140	0.215	334	0.2506	332.6

Table 2: A comparison between experimental data and neural network findings.

Location of Figure 7

The neural network was trained by changing its inter-layer weights. Finding these weights from the network and the activating functions, Equation (15) was resulted. This expression was simply how the neural network processed the input data to reach the output. A schematic presentation of the neural network is illustrated in Figure (8). In the figure IW was the layer weight and b was layer biases that after Network training specified. Furthermore, Lw was layer weight in the second layer.

The weight function, therefore, can be applied to the data without having to use and train a neural network again.

Location of Figure 8

$$output = \left(\frac{2}{1+\exp(-2(input \times IW\{1,1\} + b\{1\}))} - 1 \right) \times LW\{2,1\} + b\{2\} \qquad (15)$$

$$Iw\{1,1\} = \begin{bmatrix} -302.0717 & -41.0284 & -30.6598 & 40.5346 & 32.9756 & 23.9116 & -13.6941 \\ -58.9901 & 9.3423 & -0.5934 & 7.4534 & 0.7027 & 1.1919 & -1.9981 \end{bmatrix}$$

$$b\{1\} = \begin{bmatrix} 419.7745 & 1.2819 & 43.7335 & -57.4817 & -46.328 & -30.8861 & 19.1916 \end{bmatrix}$$

$$Lw\{2,1\} = \begin{bmatrix} 0.3161 & -0.2047 \\ -61.2159 & -141.4175 \\ 76.6069 & -498.2189 \\ -0.4292 & 0.1184 \\ 24.9429 & -160.4065 \\ -0.0303 & 0.1716 \\ 1.2058 & -0.2259 \end{bmatrix} \qquad b(2) = \begin{bmatrix} -110.8273 & 196.0753 \end{bmatrix}$$

6 Summary and Conclusions

This paper consists of two sections. First section focused on the elimination of the sphere elastic deformation from the load-penetration curve. Available techniques from other researches are based on several loading and unloading cycles which are time consuming and complex. A greatly simplified procedure was proposed in this work that provided both accuracy and simplicity. In addition to the ability of omitting elastic deformation, this technique estimated the unloading curve at each load from a single cycle load-penetration curve.

The details of determination of the stress-strain curve were provided in the second section. A two-layer neural network was trained using a series of finite element simulations and its weights were extracted explicitly. Therefore, the stress-strain curve of the material can be characterized using a single cycle load-penetration curve obtained from the sphere indentation test. A great agreement was achieved between the predicted material properties and those obtained from the experiments.

Tables

Figures

7 References

[1] M.O. Lai, K.B. Lim, On the prediction of tensile properties from hardness tests, J. Mater. Sci., 26 (1991) 2031–203.

[2] D. Tabor, The Hardness of Metals, Clarendon Press, London (1951).

[3] A.C. Fischer-Cripps, Introduction to Contact Mechanics, Mechanical Engineering Series, Springer Verlag, New York (2000).

[4] A. Nayebi, R. El Abdi, O. Bartier, G. Mauvoisin, New procedure to determine steel mechanical parameters from the spherical indentation technique, Mech. Mater., 34 (2002) 243–254.

[5] G.M. Pharr, W.C. Oliver, An improved technique for determining hardness and elastic modulus using load and displacement sensing indentation experiments. J. Mater. Res., 7 (6) (1992) 1564–1583.

[6] J.M. Collin, G. Mauvoisin, R. El Abdi, An experimental method to determine the contact radius changes during a spherical instrumented indentation, Mech. Mater., 40 (2008) 401–406.

[7] J.C. Hay, P.J. Wolff, Small correction required when applying the Hertzian contact model to instrumented indentation data. J. Mater. Res. 16 (5) (2001) 1280–1286.

[8] J.M. Collin, G. Mauvoisin, O. Bartier, R. El Abdi, P. Pilvin," Experimental evaluation of the stress–strain curve by continuous indentation using different indenter shapes" Mater. Sci. Eng. A 501 (2009) 140–145.

[9] J.M. Collin, G. Mauvoisin, P. Pilvin, R. El Abdi, Use of spherical indentation data changes to materials characterization based on a new multiple cyclic loading protocol, Mater. Sci. Eng., A 488 (2008) 608–622.

[10] E. Tyulyukovskiy, N. Huber, Identification of viscoplastic material parameters from spherical indentation data. Part I: neural networks, J. Mater. Res., 21 (2006) 664–676.

[11] E. Tyulyukovskiy, N. Huber, Neural networks for tip correction of spherical indentation curves from bulk metals and thin metal films, Journal of the Mechanics and Physics of Solids, 55 (2007) 391–418.

[12] Nikola K. Kasabov, Foundations of neural networks, fuzzy systems, and knowledge, The MIT Press, (1998).

[13] J. Kamruzzaman, R.K. Begg, R.A. Sarker, Neural networks in finance and manufacturing, Idea Group Publishing (2006).

[14] ABAQUS Users Manuals, version 6.7, Hibbit Karlsson, Sorenson Inc., 1080 Main street, Pawtucket RI, 02860-4847, USA (2006).

[15] M. Beghini, L. Bertini, V. Fontanari, Evaluation of the stress–strain curve of metallic materials by spherical indentation, Journal of Solids and Structures, 43 (2006) 2441–2459.

Figure 1

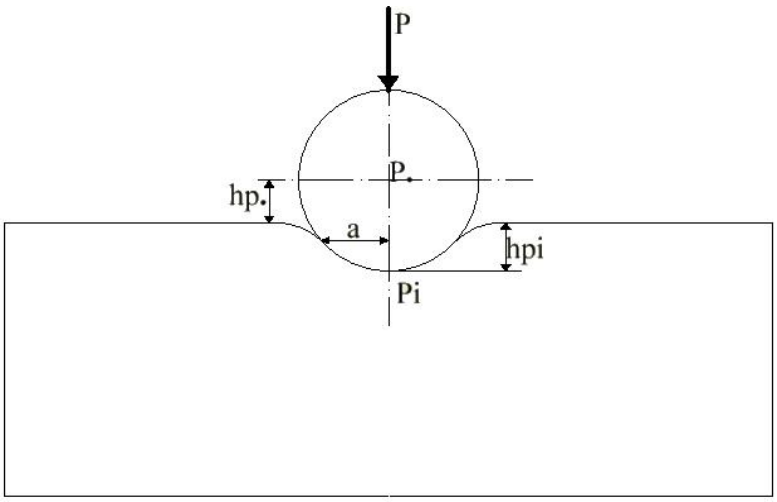

Figure 1: Difference between the measured and the real penetration.

Figure 2

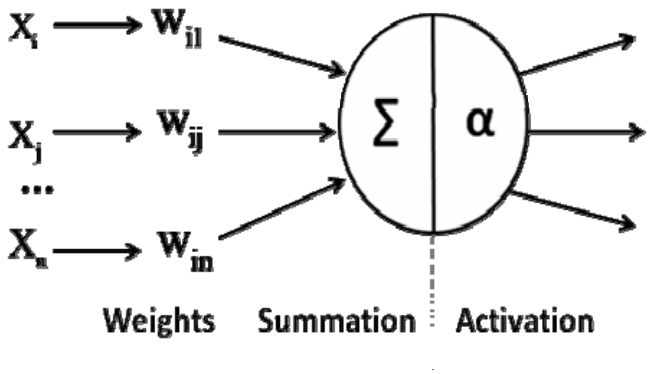

Figure 2: Data processing in a typical cell of a neural network.

Figure 3

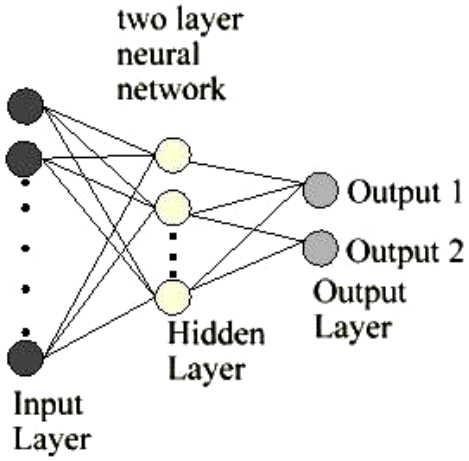

Figure 3: A two layer neural network.

Figure 4

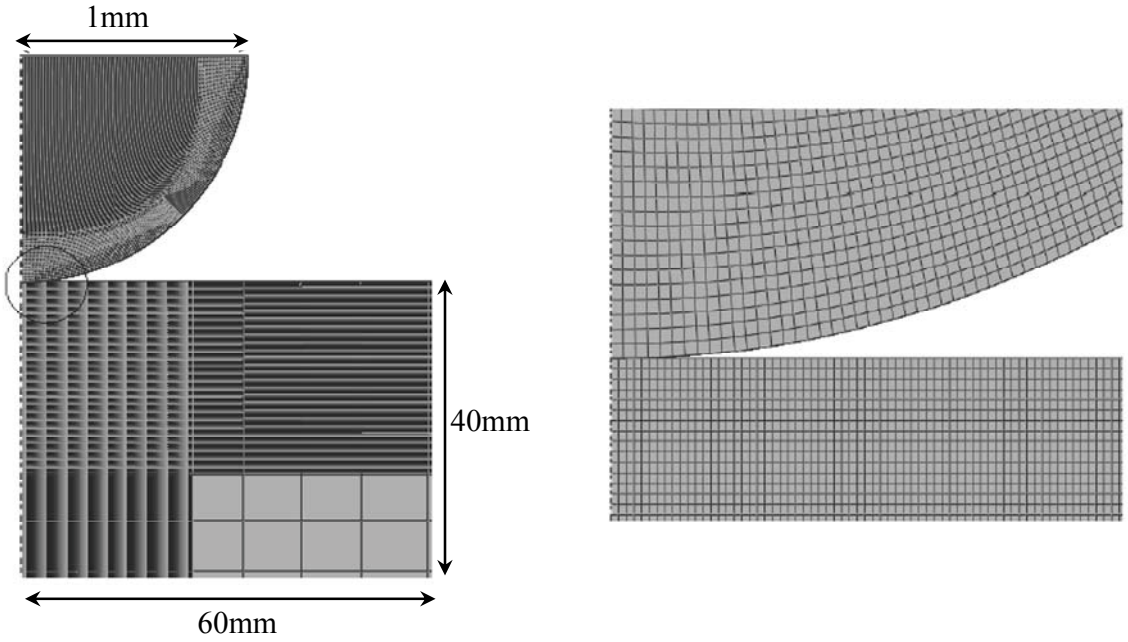

Figure 4: Finite element model used for the analysis, the presentation is not in scale.

Figure 5

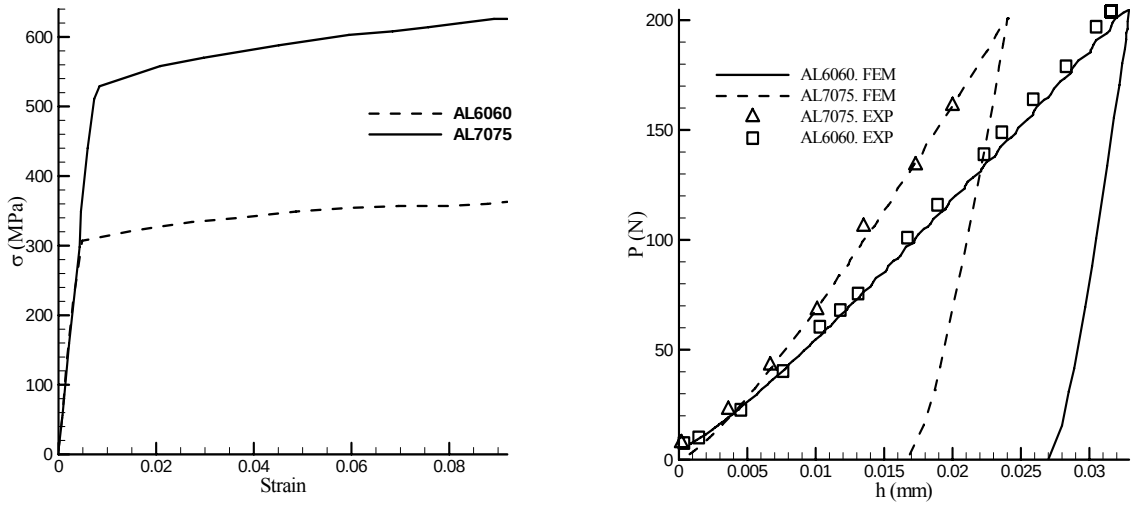

a. b.

Figure 5: (a) stress-strain curve for AL.6060 and AL.7075 [15], (b) Comparison of P-h diagram between experiment and simulation result.

Figure 6

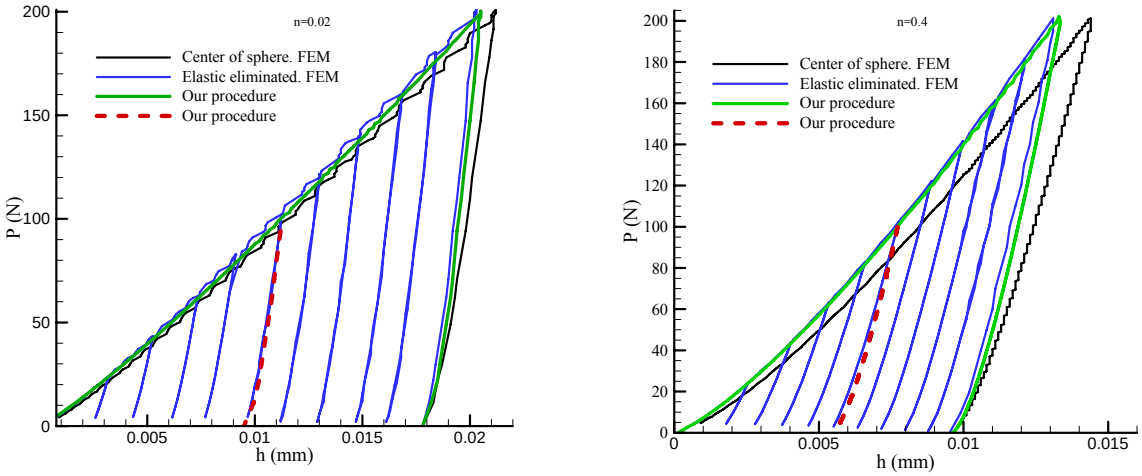

Figure 6: Load-penetration for material with $\sigma_y = 450\,Mpa,\ n = 0.02,\ n = 0.4$

Figure 7

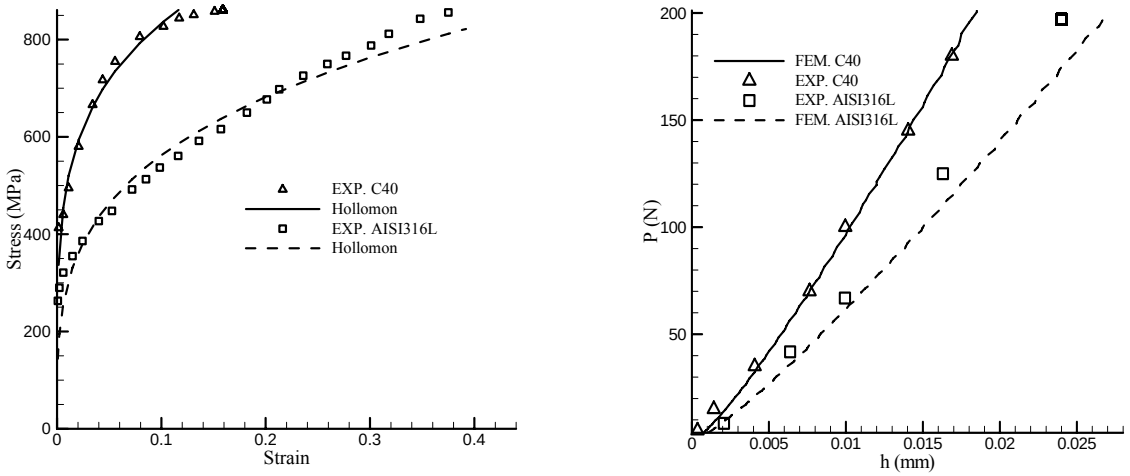

a. b.

Figure 7: (a) stress-strain curve, (b) Load-penetration curve, for C40 and AISI316L, Experimental data from [15].

Figure 8

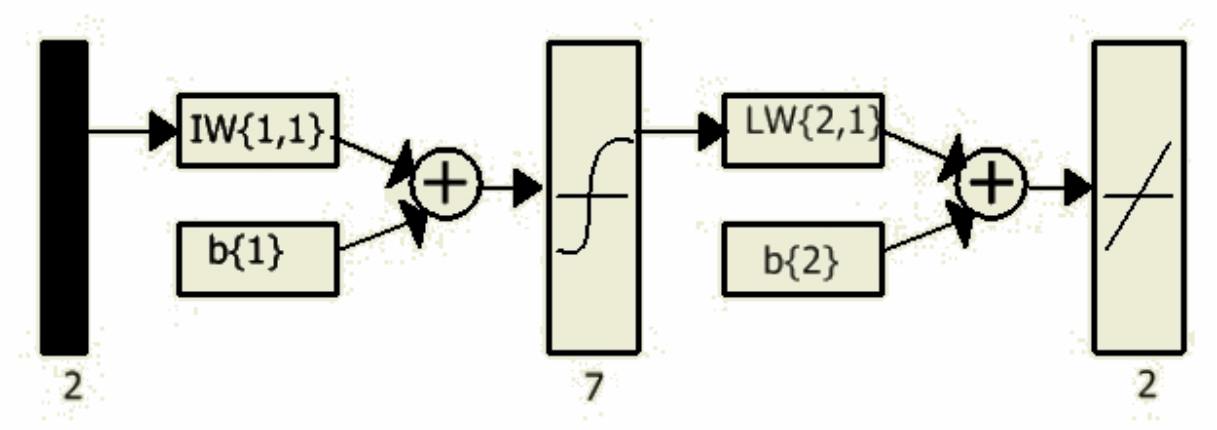

Figure 8: Neural network used with details.